

Efficient Test-Time Optimization for Depth Completion via Low-Rank Decoder Adaptation

Minseok Seo*, Wonjun Lee*, Jaehyuk Jang, and Changick Kim[†]

Korea Advanced Institute of Science and Technology (KAIST),
Daejeon, Republic of Korea
minseok.seo@kaist.ac.kr, dpenguin@kaist.ac.kr, jhyuk@kaist.ac.kr,
changick@kaist.ac.kr

*Equal contribution, [†]Corresponding author

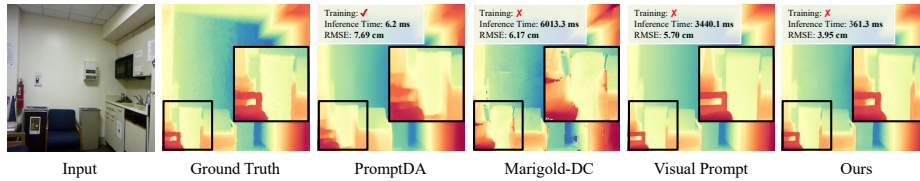


Fig. 1: We compare a training-based method (PromptDA [28]) with test-time optimization-based depth completion approaches [20, 43]. PromptDA requires sensor-specific training and achieves real-time inference, but suffers from large reconstruction error. Existing test-time optimization-based improve accuracy at the cost of several seconds of inference per image. In contrast, our method establishes a new **Pareto frontier** by simultaneously achieving the lowest error and highly efficient inference among test-time optimization-based depth completion methods.

Abstract. Zero-shot depth completion has gained attention for its ability to generalize across environments without sensor-specific datasets or retraining. However, most existing approaches rely on diffusion-based test-time optimization, which is computationally expensive due to iterative denoising. Recent visual-prompt-based methods reduce training cost but still require repeated forward-backward passes through the full frozen network to optimize input-level prompts, resulting in slow inference. In this work, we show that adapting only the decoder is sufficient for effective test-time optimization, as depth foundation models concentrate depth-relevant information within a low-dimensional decoder subspace. Based on this insight, we propose a lightweight test-time adaptation method that updates only this low-dimensional subspace using sparse depth supervision. Our approach achieves state-of-the-art performance, establishing a new Pareto frontier between accuracy and efficiency for test-time adaptation. Extensive experiments on five indoor and outdoor datasets demonstrate consistent improvements over prior methods, highlighting the practicality of fast zero-shot depth completion. Code is available at <https://wonjun-lee1009.github.io/Eff-TT0-Depth-Completion/>.

Keywords: Depth completion · Test-time optimization · Depth foundation model

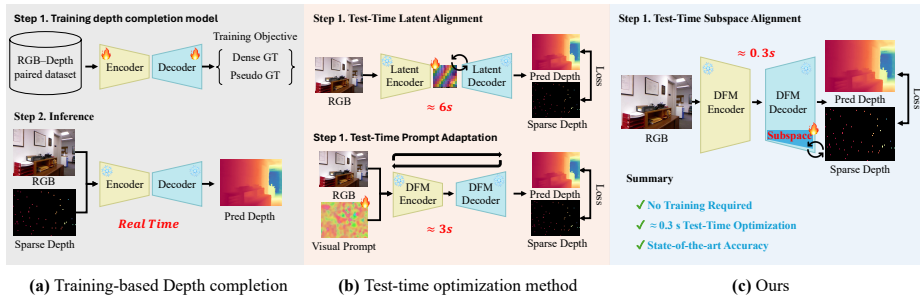


Fig. 2: (a) Training-based depth completion relies on offline training with paired RGB–depth data. (b) Test-time optimization methods adapt either latent variables or visual prompts at inference time, incurring significant computational cost. (c) In contrast, our method adapts only the decoder low-dimensional subspace, which already encodes highly correlated depth structure, enabling efficient and fast test-time adaptation.

1 Introduction

Depth estimation has become important with the emergence of modern computer vision applications, including autonomous systems [14] and 3D reconstruction [26, 44]. To obtain reliable depth predictions, information from various sensors, including RGB cameras, radar, LiDAR, and ultrasonic sensors, is commonly utilized. In particular, depth sensors such as LiDAR can provide highly accurate depth measurements at high frequency. However, due to hardware limitations the acquired depth measurements are often spatially sparse. To overcome this limitation, a large body of research has focused on estimating dense depth maps from given sparse depth measurements, a problem commonly referred to as *depth completion*. Early depth completion methods [9, 42] relied solely on sparse depth measurements to interpolate or reconstruct dense depth maps. However, they often blur or distort depth boundaries.

In contrast, RGB sensors are relatively inexpensive and widely accessible, and RGB images contain rich color and texture cues. As a result, many subsequent studies [19, 28, 34, 41, 51, 53] have leveraged RGB images as guidance to predict more accurate dense depth maps. Following this direction, training-based depth completion methods that take both RGB images and sparse depth as input have become the dominant paradigm, as illustrated in Fig. 2-(a). Although training-based methods demonstrated significant performance improvements, they require collecting sensor- and environment-specific datasets and training models accordingly, which incurs substantial cost and time for real-world deployment. Moreover, their generalization performance often degrades significantly in cross-sensor and cross-domain settings.

More recently, test-time optimization-based depth completion methods [19, 20, 38, 43] have been proposed to address these limitations, as illustrated in Fig. 2-(b). These approaches leverage depth foundation models such as Depth

Anything (v1 [46], v2 [47], and v3 [27]), Marigold [22], and UniDepth [35, 36] to generate an initial depth prediction from RGB input alone, and then optimize the output at test time using sparse depth as guidance. Such methods operate robustly across cross-sensor and cross-domain scenarios without requiring additional data collection or training, greatly improving the practicality of depth completion.

However, existing test-time optimization-based methods rely on optimization that repeatedly forwards the entire network to refine the output. As a result, they require several seconds of inference time per image. Consequently, prior work exhibits a clear trade-off between test-time optimization-based methods that are easy to deploy but slow, and training-based methods that are fast but require additional training. To resolve this trade-off, we propose Efficient Test-Time Optimization for Depth Completion via Low-Rank Decoder Adaptation, as illustrated in Fig. 2-(c).

Through a systematic analysis of encoder and decoder representations, we find that strongly depth-aligned signals concentrate in a low-dimensional subspace of the early decoder. This observation naturally motivates exploring decoder-only adaptation as an efficient design choice for test-time optimization. Based on this insight, we execute the encoder only once to extract and cache image features, and perform iterative adaptation solely through the decoder. Experiments on five indoor and outdoor datasets demonstrate that our method achieves state-of-the-art performance while delivering the fastest test-time optimization among existing zero-shot depth completion methods.

2 Related Work

2.1 Depth Foundation Models

Monocular depth estimation predicts scene depth from a single RGB image and has long been studied in computer vision. Early methods [3, 4, 8, 11, 12, 16, 18, 21, 24, 25, 48, 50] were mainly supervised on small paired RGB–depth datasets, improving via multi-scale designs, residual connections, and self-attention. However, their performance degrades under domain shifts, often requiring sensor- and environment-specific data collection and retraining, which limits zero-shot deployment.

With advances in self-supervised learning [1, 7, 17, 52] and large-scale pre-training [33, 40], depth foundation models have enabled more robust zero-shot depth estimation. MiDaS [5] showed that large-scale self-supervised visual representations can support strong cross-domain relative depth. Depth Anything [46] further improved practicality through large-scale data curation and training, accelerating adoption. In parallel, diffusion-based approaches such as Marigold [22] and GeoWizard [13] leverage pretrained generative priors to infer depth, but require iterative sampling at inference time and thus incur substantial overhead.

Recent models targeting metric depth, including Depth Anything V2 (Metric) [47], Metric3D [49], and Depth Pro [6], continue to improve accuracy, along-

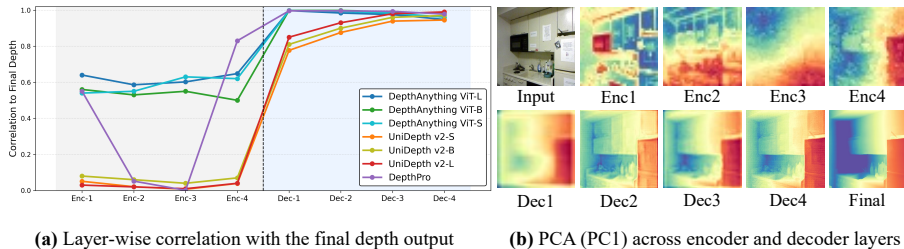


Fig. 3: (a) Layer-wise correlation with the final depth output shows low correlation in the encoder and a sharp increase in the decoder. (b) PCA (PC1) visualizations indicate that decoder features already align closely with the final depth map, revealing strong depth information in a low-dimensional decoder subspace.

side broader efforts [35, 37]. Nevertheless, current models remain fragile under severe domain shifts and often struggle to produce reliable metric depth; moreover, depth data rely on sensor-specific preprocessing and postprocessing pipelines, making cross-sensor generalization inherently difficult and motivating depth completion as a practical alternative.

2.2 Depth Completion

The dominant paradigm for depth completion is to predict a dense depth map by jointly leveraging an RGB image and sparse depth measurements. When paired RGB–depth datasets are available, training-based depth completion is a standard and effective approach [28, 34, 41, 51, 53]. However, collecting such paired data is time-consuming and costly: for RGB+LiDAR setups, sensors must be precisely calibrated and dense ground truth is often built by aggregating multiple LiDAR scans, resulting in a complex acquisition and preprocessing pipeline.

To avoid this burden, zero-shot depth completion has emerged as an alternative [20, 43]. These methods start from a pretrained depth foundation model prediction and refine it at test time using sparse depth as supervision, without additional training data. Marigold-DC [43] performs guided diffusion by injecting sparse depth constraints via test-time optimization of latent variables (with affine scale–shift alignment), achieving strong cross-domain generalization but incurring substantial inference cost due to iterative sampling.

To reduce this cost, visual prompt tuning has been explored for zero-shot depth completion [20]. While it avoids retraining on paired datasets, it still requires repeated test-time optimization over the entire network, leaving a persistent efficiency–effectiveness trade-off.

3 Analysis of Decoder Representations

The canonical pipeline of test-time optimization (TTO) for depth completion begins with an initial depth prediction from a pretrained depth foundation model

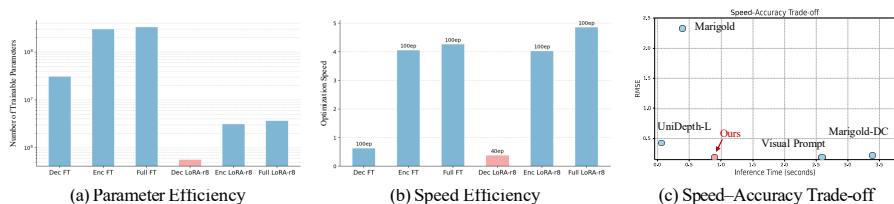


Fig. 4: Efficiency and performance comparison of test-time adaptation strategies. Decoder-only LoRA minimizes trainable parameters and adaptation time, while achieving a favorable speed–accuracy trade-off.

(DFM) given an RGB input, which is then refined using sparse depth as supervision. However, existing TTO approaches require multiple iterations of full forward passes and parameter updates at inference time, introducing seconds-level latency per image and resulting in a “high utility but slow” trade-off.

We therefore ask a fundamental question: *Where, and in what form, are the representations that most strongly influence the final depth prediction formed within a DFM?* To answer this, we analyze several representative DFMs, including Depth Anything V2 (S/B/L) [47], UniDepthV2 (S/B/L) [35], and Depth Pro [6]. For each model, we extract intermediate feature maps from multiple encoder and decoder layers and conduct two complementary analyses. First, we compute the *layer-wise correlation* between each layer representation and the final depth output to identify where depth-aligned signals become amplified across the network (Fig. 3-(a)). Second, we apply PCA to each layer feature and visualize the first principal component (PC1) as a spatial map to examine whether depth structure is broadly distributed or concentrated within a dominant low-dimensional subspace (Fig. 3-(b)). As shown in Fig. 3, a consistent pattern emerges. The layer-wise correlation remains low throughout the encoder but increases sharply upon entering the decoder (Fig. 3-(a)). Moreover, the decoder PC1 exhibits strong spatial alignment with the final depth map (Fig. 3-(b)).

This observation should not be misinterpreted as implying that the encoder is unimportant. Changes in the encoder inevitably alter the decoder inputs, and their influence propagates to the final output. Nevertheless, from the perspective of TTO design, depth-aligned signals emerge most prominently in the decoder, particularly within its low-dimensional components. These findings suggest that restricting adaptation to the decoder can provide a more *controllable and stable* [32] alternative to updating the entire model. Crucially, the computational implications are also different. Updating the encoder or the full network requires recomputing the entire forward path at each iteration. In contrast, decoder-only adaptation allows encoder features to be extracted and cached once, after which optimization proceeds solely through the decoder, significantly reducing repeated computation.

Fig. 4-(a,b) empirically validate these findings. They compare parameter efficiency and adaptation speed when applying TTO to the encoder, decoder, and

the full network. All comparisons are conducted at the best performing stable convergence epoch of each method to ensure fair evaluation. In addition, Fig. 4(c) presents a comparison in terms of accuracy and inference time against existing zero-shot depth completion methods, showing that our approach establishes a new Pareto frontier by jointly optimizing performance and efficiency.

4 Method

4.1 Problem Definition

Let $I \in \mathbb{R}^{H \times W \times 3}$ denote an RGB image, and $S \in \mathbb{R}^{H \times W}$ a sparse depth map with valid measurements only on a subset of pixels $\Omega \subseteq \{1, \dots, H\} \times \{1, \dots, W\}$. Let $D \in \mathbb{R}^{H \times W}$ denote the dense ground-truth depth, and F_θ be a depth completion model parameterized by θ . The goal of depth completion is to predict a dense depth map

$$\hat{D} = F_\theta(I, S), \quad (1)$$

where $\hat{D} \in \mathbb{R}^{H \times W}$ denotes the predicted depth.

Training-based setting. In the training-based setting, we assume access to a paired dataset $\{(I, S, D)\}$. The model parameters θ are learned by minimizing a supervised loss between the predicted depth and the dense ground truth:

$$\min_{\theta} \mathbb{E}[\mathcal{L}(F_\theta(I, S), D)]. \quad (2)$$

However, constructing paired RGB–sparse–dense datasets is often time-consuming and costly, which limits their applicability in practice.

Test-Time Optimization (TTO). When dense ground-truth depth is unavailable, test-time optimization (TTO) adapts the model at inference time using sparse depth solely as a supervision signal, rather than as an input to the model. Given a test sample (I, S) , TTO updates the model parameters by minimizing a sparse consistency loss over the observed pixel set Ω :

$$\theta' = \arg \min_{\theta} \mathcal{L}_\Omega(F_\theta(I), S), \quad (3)$$

where \mathcal{L}_Ω enforces consistency between the predicted dense depth and the sparse measurements only at the observed locations.

4.2 Decoder-Only Test-Time Optimization

We decompose a pretrained depth foundation model (DFM) F into an encoder $e(\cdot)$ and a decoder $d(\cdot)$. Given an RGB image I , the encoder is executed only once to extract a feature map $f = e(I)$. During test-time optimization, this feature representation f is kept fixed, and all subsequent adaptation is restricted to the decoder. The overall procedure of decoder-only test-time optimization is summarized in Algorithm 1.

Low-Dimensional Decoder Adaptation. As observed in Section 3, the low-dimensional representations of the decoder already exhibit strong structural

Algorithm 1: Decoder-Only Test-Time Optimization

```

Input:  $I$  (RGB),  $S$  (sparse depth),  $e, d$  (encoder, decoder)
Output:  $\hat{D}_{\text{aligned}}$ 
 $f \leftarrow e(I)$  // encode
for  $t = 1$  to  $T$  do
     $\hat{D} \leftarrow d(f)$  // decode
     $(a, b) \leftarrow \arg \min_{a, b} \sum_{(i, j) \in \Omega} (a\hat{D}_{ij} + b - S_{ij})^2$  // align
     $\hat{D}_{\text{aligned}} \leftarrow a\hat{D} + b$ 
     $\mathcal{L} \leftarrow \sum_{(i, j) \in \Omega} \|\hat{D}_{\text{aligned}, ij} - S_{ij}\|_2^2$ 
     $\theta_d \leftarrow \theta_d - \eta \nabla_{\theta_d} \mathcal{L}$  // decoder update
return  $\hat{D}_{\text{aligned}}$ 

```

correlation with the final depth prediction. Motivated by this observation, we avoid updating the entire decoder and instead restrict adaptation to its low-dimensional components. Given the fixed feature map f , the decoder produces an initial depth prediction $\hat{D} = d(f)$.

Sparse depth S is not used as an input to the model, but solely as a supervision signal at test time. However, sparse depth measurements are subject to sensor-specific biases and preprocessing variations, resulting in uncertain absolute scale and offset. Therefore, directly comparing predicted depth with sparse measurements is inappropriate.

Sparse Depth Alignment via Scale–Shift Estimation. To address this issue, we assume a linear scale–shift relationship between the predicted depth and sparse depth over the set of observed pixels Ω :

$$S_{ij} \approx a\hat{D}_{ij} + b, \quad (i, j) \in \Omega, \quad (4)$$

where a and b denote the scale and shift parameters, respectively. These parameters are estimated by minimizing the squared error over Ω using a least-squares formulation:

$$(a, b) = \arg \min_{a, b} \sum_{(i, j) \in \Omega} (a\hat{D}_{ij} + b - S_{ij})^2. \quad (5)$$

This alignment step removes the ambiguity in absolute scale inherent to sparse depth measurements and allows decoder adaptation to focus on structural consistency rather than scale matching.

Test-Time Optimization Objective. Using the estimated scale–shift parameters, we define the aligned depth prediction as

$$\hat{D}_{\text{aligned}} = a\hat{D} + b.$$

Test-time optimization then updates only the low-dimensional decoder parameters by minimizing the alignment error at sparse depth locations:

$$\min_{\theta_d} \sum_{(i, j) \in \Omega} \|\hat{D}_{\text{aligned}, ij} - S_{ij}\|_2^2. \quad (6)$$

5 Experiments

In this section, we primarily compare our method with existing zero-shot depth completion approaches. The experimental protocol follows the evaluation setup adopted in recent zero-shot depth completion literature to ensure fair comparison [20, 43]. Although our method is model-agnostic and consistently achieves stronger performance when applied to DepthAnything v2 across all benchmarks, we adopt UniDepth v2 as the primary backbone for most quantitative evaluations. This choice is made to strictly follow the protocol of [20], where UniDepth v2 is used as the standard backbone in zero-shot depth completion experiments, thereby enabling direct and fair comparison with prior work.

5.1 Experimental Settings

Evaluation Datasets. We evaluate our method on five widely used real-world datasets. These datasets collectively cover both indoor and outdoor environments, exhibit diverse image resolutions, and present varying levels of depth sparsity. Such diversity enables a comprehensive assessment of generalization across heterogeneous sensing conditions and sparse input settings.

- **IBims-1 [23]** Indoor dataset with 100 RGB–depth pairs at 640×480 . Since sparse depth is not provided, we randomly sample 1,000 points from the dense ground truth following prior protocols [20, 43].
- **VOID [45]** Indoor and outdoor RGB–depth dataset with 800 samples at 640×480 . We use 1,500 sparse depth points per image following standard evaluation settings [20, 43].
- **NYUv2 [39]** Indoor RGB–depth dataset using the official 654-sample test split. Images are resized to 304×228 , and sparse depth is constructed by randomly sampling 500 points from the dense depth [10, 11, 24, 30, 43].
- **KITTI Depth Completion (KITTI-DC) [42]** Outdoor driving dataset with RGB images and sparse LiDAR depth at 1216×352 . We evaluate on 1,000 validation samples after standard outlier filtering [24, 43].
- **DDAD [15]** Outdoor driving dataset with RGB–depth pairs at 1216×1936 . We use the front-facing camera and apply standard sparse depth outlier filtering before evaluation [24, 43].

Evaluation Metrics. Following recent zero-shot depth completion work [20, 43], we report Mean Absolute Error (MAE) and Root Mean Squared Error (RMSE) for quantitative evaluation.

Implementation Details. All experiments are conducted on a single NVIDIA H200 GPU with 140GB memory. For test-time adaptation, we adopt LoRA to enable low-dimensional tuning of the decoder while keeping the encoder fully frozen. The number of optimization iterations is set to 40, and the learning rate is fixed to 0.01. A LoRA rank of $r = 8$ is used in all experiments. All

Table 1: Comparison of training-based methods, depth foundation models, and zero-shot depth completion approaches. Zero-shot methods adapt pretrained depth foundation models at test time using sparse depth supervision without retraining. Results shown in gray are taken from Marigold-DC, while cells highlighted in green indicate the best performance.

Method	IBims-1		VOID		NYUv2		KITTI DC		DDAD	
	MAE↓	RMSE↓								
Training-based Depth Completion										
NLSPN [34] (ECCV '20)	0.049	0.191	0.210	0.668	0.440	0.716	1.335	2.076	2.498	9.231
CompletionFormer [51] (CVPR '23)	0.058	0.206	0.261	0.726	0.186	0.374	0.952	1.935	2.518	9.471
VPP4DC [2] (3DV '24)	0.062	0.228	0.148	0.543	0.077	0.247	0.413	1.609	1.344	6.781
DepthLab [29] (arXiv '24)	0.098	0.198	0.214	0.602	0.184	0.276	0.921	2.171	4.498	8.379
PromptDA [28] (CVPR '25)	0.076	0.207	0.133	0.366	0.104	0.227	1.002	3.187	0.998	3.354
PromptDA (scale shift) [28] (CVPR '25)	0.071	0.201	0.132	0.357	0.107	0.222	1.041	2.863	1.125	3.294
Depth Foundation Models										
Marigold [22] (CVPR '24)	2.785	2.972	1.294	1.523	2.315	2.466	15.450	19.093	23.640	28.456
Marigold (scale shift) [22] (CVPR '24)	0.166	0.287	0.200	0.411	0.374	0.536	1.863	3.602	5.487	8.136
UnidepthV2 [35] (CVPR '25)	0.297	0.377	0.196	0.380	0.303	0.422	1.502	3.191	2.933	5.362
UnidepthV2 (scale shift) [35] (CVPR '25)	0.097	0.203	0.141	0.343	0.144	0.250	1.395	2.837	4.312	6.411
Zero-shot Depth Completion										
Marigold-DC [43] (ICCV '25)	0.061	0.189	0.106	0.322	0.093	0.216	0.568	1.663	1.795	4.141
UnidepthV2+TestPromptDC [20] (ICCV '25)	0.062	0.201	0.103	0.306	0.111	0.186	0.548	1.793	4.263	6.433
UnidepthV2+Ours	0.041	0.138	0.086	0.271	0.109	0.182	0.515	1.476	2.012	4.160

hyperparameters are kept identical across datasets, without any dataset-specific tuning.

For the main quantitative results and all ablation studies, we use UniDepthV2-L as the backbone, following the setting of TestPromptDC [20], which applies input-level visual prompt tuning and represents the current state-of-the-art baseline. All experiments are reproduced strictly following the official code released by the original authors to ensure fairness and consistency.

5.2 Main Results

Comparison with Other Methods Tab 1 compares training-based depth completion methods, depth foundation models (DFMs), and zero-shot depth completion approaches. Directly applying DFMs to sparse depth inputs leads to degraded performance, as they struggle to recover accurate metric depth despite strong monocular priors. In contrast, incorporating sparse depth as test-time supervision consistently reduces errors across zero-shot methods, indicating that DFMs already encode rich geometric structure. The remaining challenge is therefore not representational capacity, but scale ambiguity and sensor-specific mismatch arising from hardware, calibration, and preprocessing differences. Our method directly addresses this issue by selectively adapting a low-dimensional decoder subspace that is strongly correlated with the final depth prediction. This targeted adaptation effectively resolves scale inconsistency and structural misalignment, achieving state-of-the-art performance on most datasets.

Inference Speed Comparison Tab 2 reports the inference time (in seconds) across different input resolutions (VGA, SD, HD, and FHD). Since depth foundation models (DFMs) do not involve test-time optimization, they exhibit low

Table 2: Comparison of inference time (seconds) with respect to input image size. The inference speed of DFMs is reported for reference only, as they do not involve test-time optimization. Our primary comparison focuses on test-time optimization methods.

Resolution	Depth Foundation Model		Test-time Optimization		
	Marigold	UnidepthV2	Marigold-DC	UnidepthV2+TestPromptDC	UnidepthV2+Ours
VGA	0.49	0.04	9.74	7.27	0.54
SD	0.56	0.04	10.47	8.19	0.61
HD (720p)	1.43	0.05	18.47	26.79	1.24
FHD (1080p)	4.20	0.05	42.82	79.35	2.53

Table 3: Ablation study on robustness to sparse depth supervision. We evaluate zero-shot depth completion methods across different sparsity regimes on NYUv2 and varying LiDAR channel densities on KITTI-DC.

Method	NYUv2 100 samples		NYUv2 50 samples		NYUv2 5 samples		KITTI-DC 32 channels		KITTI-DC 16 channels		KITTI-DC 8 channels		KITTI-DC 4 channels	
	MAE↓	RMSE↓	MAE↓	RMSE↓	MAE↓	RMSE↓	MAE↓	RMSE↓	MAE↓	RMSE↓	MAE↓	RMSE↓	MAE↓	RMSE↓
	Marigold-DC	0.154	0.308	0.192	0.354	0.426	0.594	0.621	1.875	0.739	2.199	0.924	2.586	1.182
PromptDA	0.148	0.288	0.192	0.341	0.610	0.848	1.069	3.377	1.223	1.223	1.527	4.475	1.861	4.642
PromptDA (scale shift)	0.152	0.280	0.194	0.333	0.610	0.848	1.096	3.030	1.227	3.396	1.475	3.999	1.816	4.143
TestPromptDC	0.101	0.217	0.115	0.235	0.553	0.658	0.562	1.866	0.605	2.044	0.701	2.327	0.814	2.483
Ours	0.119	0.205	0.127	0.219	0.233	0.343	0.541	1.592	0.591	1.776	0.684	2.049	0.828	2.347

inference latency. In contrast, test-time optimization methods such as Marigold-DC and visual prompting incur substantial overhead, already requiring 8–9 seconds at VGA resolution. Our method achieves significantly lower latency among TTO approaches, running in approximately 2 seconds at VGA. As resolution increases, Marigold-DC scales poorly (up to 42 seconds at FHD), while visual prompting fails due to out-of-memory errors. In comparison, our method remains feasible at FHD with an inference time of 15 seconds. Overall, our approach is the fastest among test-time optimization methods, while also achieving the best depth completion performance across all evaluated models.

5.3 Ablation Study

Robustness to Depth Sparsity Tab 3 presents the generalization performance of zero-shot depth completion methods with respect to the number of available sparse depth samples. To evaluate robustness across different environments, we conduct experiments on both an indoor dataset (NYUv2) and an outdoor dataset (KITTI-DC).

Our method exhibits a similar performance trend to other zero-shot depth completion approaches as the number of depth samples increases. Specifically, performance consistently improves with more available depth measurements, indicating that all methods benefit from denser supervision. Importantly, across all sparsity regimes and in both indoor and outdoor settings, our method consistently outperforms competing zero-shot depth completion methods. This demonstrates that the proposed decoder-only adaptation strategy remains effective and

Table 4: Backbone generalization across model families. We evaluate our method on UniDepthV2 and DepthAnythingV2 backbones with S/B/L model sizes.

(a) UniDepthV2					(b) DepthAnythingV2						
Size	Method	NYUv2		KITTI		Size	Method	NYUv2		KITTI	
		MAE↓	RMSE↓	MAE↓	RMSE↓			MAE↓	RMSE↓	MAE↓	RMSE↓
S	Base	0.434	0.537	2.651	4.261	S	Base	1.371	1.471	2.179	4.157
	Base (scale shift)	0.172	0.275	1.400	2.988		Base (scale shift)	0.246	0.358	1.960	3.822
	TestPromptDC	0.081	0.179	0.579	1.927		TestPromptDC	0.091	0.186	0.527	1.614
	Ours	<u>0.135</u>	<u>0.213</u>	<u>0.646</u>	1.699		Ours	0.067	0.133	<u>0.558</u>	1.484
B	Base	0.382	0.490	1.387	2.994	B	Base	1.183	1.286	1.247	3.929
	Base (scale shift)	0.155	0.260	1.289	2.811		Base (scale shift)	0.219	0.325	1.806	3.531
	TestPromptDC	0.083	0.187	0.636	2.146		TestPromptDC	0.090	0.186	0.499	1.584
	Ours	<u>0.109</u>	0.185	0.581	1.518		Ours	0.060	0.126	0.469	1.410
L	Base	0.303	0.422	1.502	3.191	L	Base	1.160	1.258	2.301	3.980
	Base (scale shift)	0.143	0.250	1.009	2.474		Base (scale shift)	0.205	0.310	1.701	3.293
	TestPromptDC	0.111	0.186	0.548	1.793		TestPromptDC	0.094	0.193	0.504	1.580
	Ours	0.109	0.182	0.515	1.476		Ours	0.058	0.124	0.433	1.389

robust regardless of the sparsity level of the input depth measurements or the underlying scene domain.

Backbone Generalization Tab 4 reports generalization performance across different depth foundation model backbones and model sizes. We evaluate our method on UniDepthV2 and DepthAnythingV2 with S/B/L variants. Across both backbone families, our method consistently improves performance over the corresponding base models, despite differences in architecture and training protocols. Notably, the performance gains become more pronounced as model size increases. For DepthAnythingV2, our method outperforms the baseline across all S/B/L variants, with larger backbones exhibiting stronger improvements. This suggests that larger depth foundation models encode richer depth-aligned structure in the decoder, which can be more effectively exploited by our low-dimensional adaptation strategy.

An exception is observed for UniDepthV2-S, where visual prompt tuning slightly outperforms our method, likely due to the limited representational capacity of smaller backbones. Nevertheless, as model capacity increases, our decoder-only adaptation becomes increasingly effective and consistently surpasses alternative test-time optimization strategies. Finally, we note that our approach is designed for estimation-based depth foundation models and is not directly applicable to generation-based methods such as diffusion-based depth generation.

Learning Rate and Epoch Analysis We conduct experiments on NYUv2 to identify an appropriate learning rate for test-time adaptation. Specifically, we compare learning rates of 0.01, 0.001, and 0.0001. As shown in Fig. 5-(a), our method converges rapidly with a learning rate of 0.01 and reaches stable performance around 40 epochs. Based on this observation, we fix the number of adaptation epochs to 40 in all main experiments. In contrast, lower learning rates require substantially more iterations to converge, without providing additional performance improvements.

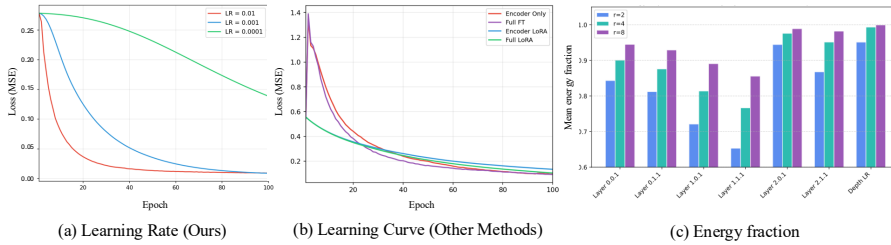


Fig. 5: Energy fraction captured by low-rank components of decoder weight updates. Most layers exhibit strongly low-rank structures, where rank $r = 8$ explains over 90% of the total energy.

Table 5: Ablation study on adaptation strategy and LoRA rank on NYUv2.

(a) Adaptation Scope				(b) LoRA Rank Sensitivity		
Method	MAE↓	RMSE↓	Total Time↓	Rank r	MAE↓	RMSE↓
Encoder-only FT	0.162	0.268	7651s	2	0.126	0.213
Decoder-only FT	0.129	0.221	2406s	4	0.111	0.186
Full FT (Enc+Dec)	0.148	0.247	7972s	8	0.109	0.181
Encoder-only LoRA	0.112	0.193	6428s	16	0.115	0.195
Decoder-only LoRA	0.109	0.181	1074s	32	0.121	0.204
Full LoRA (Enc+Dec)	0.112	0.197	7084s			

For a fair comparison, we evaluate encoder-only fine-tuning, full fine-tuning, encoder-only LoRA, and full LoRA under the same epoch setting. However, as illustrated in Fig. 5-(b), these alternative strategies require up to 100 epochs to reach stable convergence. Moreover, they achieve their best performance only with a smaller learning rate of 0.0001, while larger learning rates such as 0.01 and 0.001 lead to unstable optimization and degraded accuracy. (see supplementary material) These results indicate that decoder-only LoRA adaptation is relatively stable, allowing the use of a larger learning rate and enabling faster convergence during test-time optimization.

Relation Between LoRA and Low-Dimensional Features. To analyze why low-rank adaptation is effective for decoder-only test-time optimization, we examine how weight updates from full fine-tuning are distributed across low-dimensional subspaces. For each input sample, we fine-tune a single decoder layer while freezing all others, and compute the weight difference Δ . Applying SVD to Δ , we measure the fraction of energy captured by the top- r singular values.

As shown in Fig. 5-(c), most decoder layers exhibit highly concentrated energy in a few dominant directions. In particular, rank $r = 4$ already captures over 80% of the energy in most layers, while rank $r = 8$ consistently explains more than 90%, and in some cases nearly all of the energy. This indicates that meaningful test-time adaptation naturally lies in a low-dimensional subspace, providing strong justification for LoRA-based adaptation.

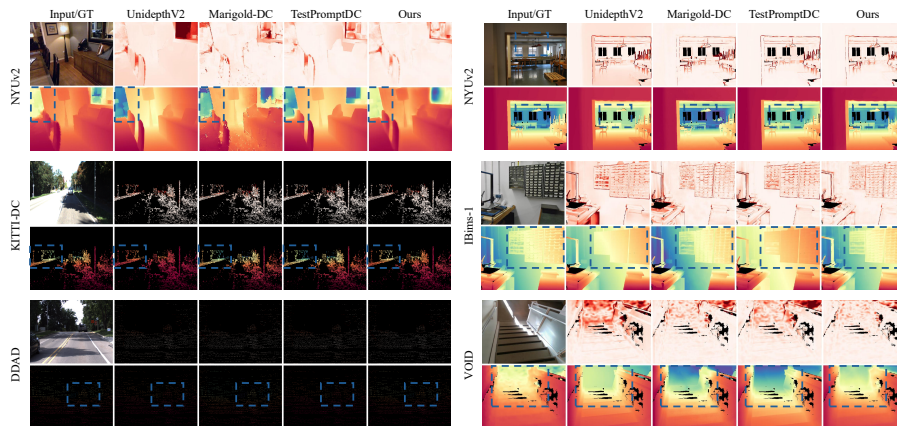


Fig. 6: Qualitative results on multiple datasets. For each dataset, the top row shows the error maps with respect to the ground truth, and the bottom row shows the corresponding depth predictions. Blue dashed boxes highlight representative regions for easier comparison; readers are encouraged to zoom in for detailed inspection.

Impact of Adaptation Strategies. We conduct an ablation study on the NYUv2 dataset to analyze the effect of different adaptation strategies, including encoder-only fine-tuning, decoder-only fine-tuning, full fine-tuning, encoder-only LoRA, decoder-only LoRA, and full LoRA.

For decoder-only LoRA, we adopt a learning rate of 0.01 and 40 optimization epochs, as this configuration achieves both the best performance and the fastest stable convergence. In contrast, the other adaptation strategies are trained with a learning rate of 0.001 for 100 epochs, since they require substantially more iterations to reach stable convergence and attain their best performance. Each method is evaluated under its best-performing stable configuration to ensure a fair comparison. As shown in Tab 5-(a), decoder-only LoRA achieves both the highest accuracy and the fastest adaptation. Owing to the significantly reduced number of trainable parameters, it remains stable even with a larger learning rate, enabling rapid convergence within fewer epochs. These factors collectively result in superior efficiency-accuracy trade-offs. Tab 5-(b) presents the sensitivity analysis with respect to the LoRA rank. We observe that a moderate rank of $r = 8$ yields the best performance, while both smaller and larger ranks lead to inferior results.

6 Qualitative Results

As shown in Fig. 6, our method achieves more effective structural correction by directly adapting the decoder weights that generate the final depth map. Unlike input- or feature-level conditioning approaches, such as visual prompting or feature modification, which alter input representations or intermediate

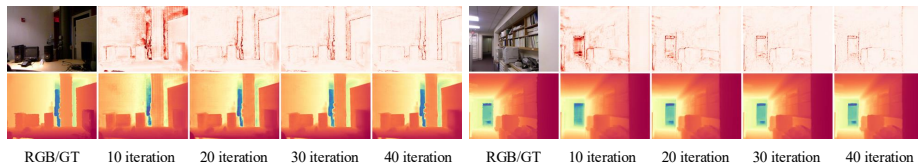


Fig. 7: Error maps and depth predictions over optimization iterations. The top row visualizes the error maps, while the bottom row presents the corresponding predicted depth maps.

features while keeping the depth prediction function fixed, our approach operates in the decoder parameter space that governs metric scale and geometric structure. This enables more direct resolution of scale inconsistency and structural misalignment, resulting in sharper and more coherent depth predictions, particularly in regions with sparse or missing depth measurements.

Fig. 7 illustrates the error maps across optimization iterations. In the early iterations, visible artifacts and structural inconsistencies remain. As optimization progresses, these artifacts are gradually reduced, leading to cleaner and more geometrically consistent depth predictions in later iterations.

7 Limitation and Future Work

Although our method achieves the best performance and the fastest inference among existing single-image zero-shot depth completion approaches, it still relies on test-time parameter updates and thus does not yet operate in strict real-time. A promising future direction is to extend our framework to video-based depth completion, where adapted decoder parameters can be reused across consecutive frames. By exploiting temporal coherence, the optimization cost can be amortized over time, potentially enabling near real-time or real-time deployment.

8 Conclusion

In this work, we analyzed the relationship between intermediate representations of depth foundation models and their final depth predictions. Through layer-wise correlation and PCA analyses, we showed that strongly depth-aligned signals emerge predominantly in the decoder and are concentrated within a low-dimensional subspace. Motivated by this observation, we proposed *Low-Rank Decoder Adaptation*, a lightweight test-time optimization method that updates only the decoder’s low-dimensional parameters using sparse depth supervision. By restricting adaptation to a compact and depth-relevant subspace, our method achieves state-of-the-art performance among zero-shot depth completion approaches while significantly reducing computational and parameter overhead. We hope that our findings provide useful insights into the design of efficient

test-time adaptation strategies and contribute to making zero-shot depth completion more practical for real-world applications.

A Supplementary Overview

This supplementary material provides additional details and analyses that complement the main paper. For clarity, we summarize the main purpose of each section below:

- **Important implementation details.** This section summarizes several implementation choices that are important for fair and reproducible evaluation.
- **Additional Runtime and Memory Results without Deterministic Constraints.** The main paper reports runtime and memory under deterministic settings for reproducibility. In contrast, this supplementary material additionally presents results obtained without deterministic constraints, reflecting a more practical execution scenario.
- **Additional Results on Depth AnythingV2.** We report additional experimental results based on Depth AnythingV2.
- **Additional Qualitative Results.** We present further qualitative examples that were omitted from the main paper due to space limitations.
- **Detailed Experimental Settings and Protocol Rationale.** We provide the detailed experimental settings used in the main paper and clarify the rationale behind key protocol choices.
- **Empirical Analysis of Low-Rank Structure and PCA.** This section examines how the low-dimensional principal subspace of decoder features relates to the observed low-rank structure of test-time adaptation.
- **A Local Linearized Interpretation of Low-Rank Update Structure.** We provide an additional analysis of the relationship between low-rank feature structure and low-rank weight adaptation. Rather than aiming for a complete theory of nonlinear adaptation dynamics, this section offers a local linearized interpretation that is consistent with our empirical observations.

B Important Implementation Details

For all datasets, we resize the input resolution so that both height and width are divisible by 14. This is required by the patch size of the DINOv2 backbone, and the same practice is also followed by prior methods [20]. For TestPromptDC in particular, resolutions larger than approximately 1280×720 lead to out-of-memory (OOM) errors. Therefore, for high-resolution datasets such as DDAD, we resize the input to a resolution close to 1274×728 . To ensure reproducibility, we provide the code used for all experiments in the supplementary material. Additional implementation details can be found in the accompanying code.

Table 6: Total adaptation time for 40 iterations across different backbones and input resolutions. Lower is better.

Backbone	TestPromptDC					Encoder-Only					Decoder-Only				
	224	VGA	SD	HD	FHD	224	VGA	SD	HD	FHD	224	VGA	SD	HD	FHD
Depth AnythingV2-S	0.61	0.88	0.98	3.41	21.58	0.82	1.11	1.21	3.80	22.33	0.20	0.18	0.19	0.34	0.60
Depth AnythingV2-B	0.52	1.78	1.99	7.42	44.66	0.70	2.35	2.59	8.52	46.76	0.17	0.26	0.28	0.55	1.06
Depth AnythingV2-L	1.07	4.45	5.25	20.30	OOM	1.67	5.90	6.82	23.58	OOM	0.28	0.49	0.55	1.15	2.34
UniDepthV2-S	0.69	0.96	1.08	3.72	23.14	0.91	1.20	1.33	4.08	23.97	0.23	0.21	0.22	0.39	0.69
UniDepthV2-B	0.59	1.92	2.16	7.95	46.85	0.79	2.51	2.77	8.96	48.72	0.20	0.29	0.31	0.60	1.18
UniDepthV2-L	1.18	4.78	5.61	21.44	74.92	1.82	6.26	7.18	24.91	79.35	0.31	0.54	0.61	1.24	2.53

Table 7: Peak GPU memory usage (MB) during adaptation across different backbones and input resolutions. Lower is better.

Backbone	TestPromptDC					Encoder-Only					Decoder-Only				
	224	VGA	SD	HD	FHD	224	VGA	SD	HD	FHD	224	VGA	SD	HD	FHD
Depth AnythingV2-S	374	1588	1854	8645	40572	673	1981	2272	9419	42231	421	673	707	1274	2429
Depth AnythingV2-B	1027	3562	4067	17682	81485	2153	4677	5241	19455	85064	1347	1754	1821	2806	4805
Depth AnythingV2-L	3146	9771	11052	43854	OOM	7289	13317	14755	48922	OOM	4280	5007	5123	6904	10554
UniDepthV2-S	462	1418	1597	5824	10863	781	1686	1864	6415	11692	508	712	751	1268	2187
UniDepthV2-B	1184	3187	3498	9612	12844	2367	3841	4175	10493	13628	1412	1716	1779	2598	3972
UniDepthV2-L	2986	6215	6682	11877	13652	6418	7542	8019	12736	OOM	3897	4316	4471	5968	8127

C Additional Runtime and Memory Results without Deterministic Constraints.

Speed comparison. Table 6 reports the total adaptation time in seconds. The results show that decoder-only adaptation is consistently the fastest test-time optimization strategy across different backbone sizes and input resolutions. This is mainly because our method runs the encoder only once, caches the extracted image features, and performs all subsequent optimization steps only through the decoder. In contrast, TestPromptDC and encoder-only adaptation repeatedly recompute the encoder during test-time optimization, which leads to substantially higher computational cost. As a result, the runtime gap becomes increasingly pronounced as the input resolution and model size grow.

We also observe that, at very small resolutions such as 224×224 , Depth AnythingV2-B can be slightly faster than Depth AnythingV2-S under TestPromptDC. We attribute this behavior to hardware-level benchmarking effects rather than a genuine reversal of computational efficiency. When the input resolution is very small, fixed overheads such as kernel launch latency, optimizer steps, and autograd bookkeeping can dominate the measured runtime, and a slightly larger model may occasionally achieve better GPU utilization. As the input resolution increases, however, the expected scaling trend becomes clear, and the smaller backbone is consistently faster.

Memory Comparison. Table 7 shows that decoder-only adaptation is also substantially more memory-efficient than TestPromptDC and encoder-only adapta-

Table 8: Comparison of training-based methods, depth foundation models, and zero-shot depth completion approaches. Zero-shot methods adapt pretrained depth foundation models at test time using sparse depth supervision without retraining. Results shown in gray are taken from Marigold-DC, while cells highlighted in green indicate the best performance.

Method	IBims-1		VOID		NYUv2		KITTI DC		DDAD	
	MAE↓	RMSE↓								
Training-based Depth Completion										
NLSPN [34] (ECCV '20)	0.049	0.191	0.210	0.668	0.440	0.716	1.335	2.076	2.498	9.231
CompletionFormer [51] (CVPR '23)	0.058	0.206	0.261	0.726	0.186	0.374	0.952	1.935	2.518	9.471
VPP4DC [2] (3DV '24)	0.062	0.228	0.148	0.543	0.077	0.247	0.413	1.609	1.344	6.781
DepthLab [29] (arXiv '24)	0.098	0.198	0.214	0.602	0.184	0.276	0.921	2.171	4.498	8.379
PromptDA [28] (CVPR '25)	0.076	0.207	0.133	0.366	0.104	0.227	1.002	3.187	0.998	3.354
PromptDA (scale shift) [28] (CVPR '25)	0.071	0.201	0.132	0.357	0.107	0.222	1.041	2.863	<u>1.125</u>	3.294
Depth Foundation Models										
Marigold [22] (CVPR '24)	2.785	2.972	1.294	1.523	2.315	2.466	15.450	19.093	23.640	28.456
Marigold (scale shift) [22] (CVPR '24)	0.166	0.287	0.200	0.411	0.374	0.536	1.863	3.602	5.487	8.136
DepthAnythingV2 [35] (CVPR '25)	0.387	0.472	0.292	0.472	1.160	1.258	2.301	3.980	3.739	6.706
DepthAnythingV2 (scale shift) [35] (CVPR '25)	0.129	0.224	0.159	0.357	0.205	0.310	1.701	3.293	2.966	5.504
Zero-shot Depth Completion										
Marigold-DC [43] (ICCV '25)	0.061	0.189	0.106	0.322	0.093	0.216	0.568	1.663	1.795	4.141
DepthAnythingV2+TestPromptDC [20] (ICCV '25)	0.063	0.194	0.098	0.299	0.094	0.193	0.504	1.580	-	-
DepthAnythingV2+Ours	0.046	0.137	0.095	<u>0.325</u>	0.058	0.124	0.433	1.389	1.751	4.388

tion across nearly all backbone sizes and input resolutions. This benefit arises for the same architectural reason. Since our method caches the encoder features and restricts optimization to the decoder, it avoids storing intermediate activations and gradients for repeated encoder updates, which significantly reduces GPU memory consumption during test-time optimization.

As the backbone size and input resolution increase, this memory advantage becomes even more pronounced. In particular, for Depth AnythingV2-L at FHD resolution, both TestPromptDC and encoder-only adaptation result in out-of-memory errors, whereas decoder-only adaptation remains feasible. These results show that the memory bottleneck of test-time optimization mainly comes from repeatedly optimizing the encoder, and that removing this bottleneck leads to much better scalability in practice.

D Additional Results on Depth AnythingV2

Accuracy Comparison. Tab 8 presents the quantitative comparison results on Depth AnythingV2-L. Compared with the results on UniDepthV2, our method achieves an even larger performance margin over prior approaches, further establishing a new state of the art. These results suggest that our decoder-only adaptation strategy is not specific to a single backbone, but generalizes effectively across different depth foundation models.

E Additional Qualitative Results

The examples in Fig. 8 are randomly sampled rather than selectively chosen. Across a wide range of datasets, our method generally produces the most accurate and visually consistent depth predictions. In particular, our results tend to

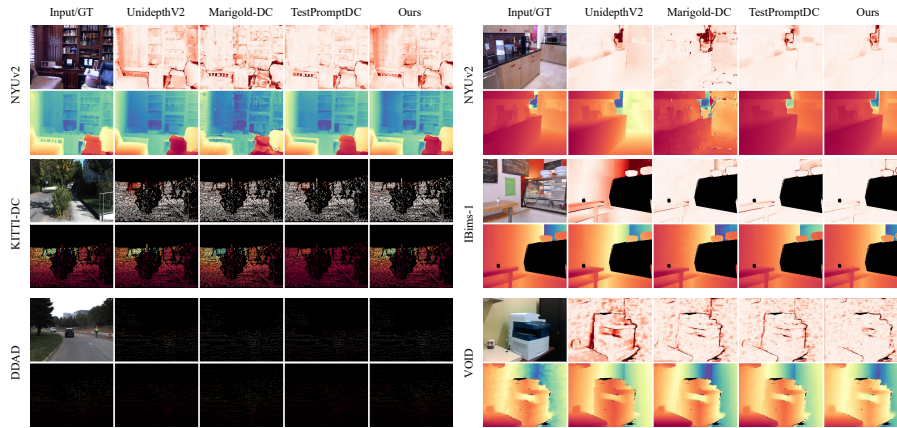


Fig. 8: Qualitative results on multiple datasets. For each dataset, the top row shows the error maps with respect to the ground truth, and the bottom row shows the corresponding depth predictions.

preserve object boundaries more reliably and show fewer severe local artifacts than prior zero-shot baselines. We further observe that Marigold-DC can become unstable on some samples, occasionally producing visibly degraded predictions. By contrast, our method remains consistently stable across samples and yields more reliable predictions overall.

F Detailed Experimental Settings and Protocol Rationale.

Clarification of figures, tables, and evaluation protocols. The figures and tables in the main paper are designed for different comparison purposes, and the choice of backbone is determined accordingly. For clarity, we summarize the role of each figure and table below.

- **Figure 1: Trade-off between training-based and test-time optimization methods.** The purpose of Fig. 1 is to illustrate the practical trade-off between training-based depth completion methods and test-time optimization (TTO) methods. To make this comparison as fair as possible, we use Depth AnythingV2-L as the common backbone whenever applicable. In particular, this choice is motivated by the fact that PromptDA is also built on top of Depth AnythingV2-L. Under this matched-backbone setting, Fig. 1 highlights that our method achieves the best reconstruction accuracy among the compared methods, while also being the fastest among TTO-based approaches. Therefore, the figure is intended to emphasize the accuracy-efficiency trade-off between training-based methods and TTO methods under a practically aligned comparison protocol.

- **Figure 2: Visual comparison of different adaptation paradigms.** Fig. 2 is intended to provide an intuitive comparison of representative adaptation paradigms. Panel (a) corresponds to the PromptDA-style training-based paradigm. In panel (b), the upper example corresponds to Marigold-DC, and the lower example corresponds to TestPromptDC. Panel (c) presents our method. As in Fig. 1, we use Depth AnythingV2-L in comparisons involving PromptDA-style methods, so that the visual comparison remains consistent with the matched-backbone setting. The goal of this figure is not to serve as a benchmark table, but to visually clarify the difference between training-based adaptation, prior test-time optimization strategies, and our decoder-only adaptation framework.
- **Table 1: Quantitative comparison with prior test-time optimization methods.** The purpose of Table 1 is to provide the main quantitative comparison with prior zero-shot depth completion methods, especially previous state-of-the-art TTO approaches. For this reason, we follow the evaluation protocol of TestPromptDC and use UniDepthV2 as the backbone in this table. This enables the most direct and controlled comparison with the strongest prior TTO baseline under the standard protocol used in recent literature.
- **Re-evaluation of TestPromptDC.** During our reproduction, we found that the official implementation of TestPromptDC uses ground-truth information during the scale-alignment step in test-time optimization. Since such information should not be available in a proper zero-shot test-time adaptation setting, we regard this as an inappropriate evaluation design for fair comparison. Therefore, in our experiments, we re-evaluate TestPromptDC after removing this ground-truth-dependent component. The resulting performance is lower than originally reported, and we believe this corrected protocol provides a fairer and more reliable comparison.
- **Why PromptDA-based results can appear particularly strong.** PromptDA takes as input a dense low-resolution depth condition, which is more informative than directly using sparse depth samples. By contrast, many prior methods are designed to operate directly from sparse depth inputs. To provide PromptDA with an appropriate input format, we first convert sparse depth into a dense low-resolution depth map through interpolation, and then use it as the input condition. This substantially improves performance, and helps explain why PromptDA-based methods can appear particularly strong relative to methods that are evaluated from raw sparse depth alone.
- **Table 2: Runtime comparison under deterministic settings.** The runtime results reported in Table 2 of the main paper are measured under **deterministic settings** to ensure reproducibility. Since deterministic execution may introduce additional overhead, these measurements can be slower than those obtained in a more practical non-deterministic setting. For completeness, the supplementary material additionally reports runtime without deterministic constraints. As shown in Supplementary Table 2, the runtime of our method becomes even faster in this practical setting. Nevertheless,

Table 9: PCA-subspace projection ablation on NYUv2 using decoder-only LoRA.

Setting	Subspace Dim.	MAE ↓	RMSE ↓
No feature projection	Full	0.109	0.181
Top-PC only	4	0.116	0.194
Top-PC only	8	0.112	0.187
Top-PC only	16	0.110	0.183
Orthogonal to Top-8	Full-8	0.125	0.214
Orthogonal to Top-16	Full-16	0.128	0.220
Random subspace	8	0.121	0.205
Random subspace	16	0.118	0.199

we intentionally report the deterministic-setting runtime in the main paper, since it provides a more reproducible and conservative comparison.

G Empirical Analysis of Low-Rank Structure and PCA

In this section, we provide additional empirical evidence linking the low-dimensional structure of decoder features to the effectiveness of low-rank adaptation. While the main paper shows that decoder representations exhibit strong alignment with the final depth prediction and that decoder weight updates are highly low-rank, the following analyses further examine whether these two observations are functionally connected. To this end, we conduct two additional studies: 1) PCA-subspace projection ablations, and 2) alignment analysis between feature covariance and weight-update spectra.

PCA Subspace Projection Ablation. To test whether the principal decoder subspace is functionally important for adaptation, we project decoder features onto different subspaces during test-time optimization. Specifically, we compare four settings: no feature projection, projection onto the top- k principal subspace, projection onto its orthogonal complement, and projection onto a random subspace of the same dimension. If the low-rank decoder structure is genuinely responsible for effective adaptation, most of the adaptation gain should be preserved within the top principal subspace, whereas the orthogonal and random subspaces should lead to substantially weaker adaptation.

As shown in Table 9, restricting adaptation to the top principal subspace preserves most of the performance gain of the default decoder-only LoRA setting. In contrast, projecting features onto the orthogonal complement or onto a random subspace leads to substantially weaker performance. These results suggest that adaptation-relevant information is concentrated in a low-dimensional principal subspace of decoder features. Notably, even a relatively small principal subspace already recovers most of the benefit of the default setting, supporting the view that decoder adaptation is effectively low-dimensional.

Alignment Between Feature Covariance and Weight Updates. We next examine whether the low-rank structure of decoder features is directly reflected in the weight updates induced by adaptation. For each decoder layer, we compute the feature covariance spectrum and the singular value spectrum of the

Table 10: Alignment between decoder feature covariance and update spectra on NYUv2.

Layer	Feature Top-8 Energy \uparrow	Update Top-8 Energy \uparrow	Cosine Sim. \uparrow	Rank-8 MAE \downarrow
Decoder Stage 1	0.88	0.81	0.73	0.118
Decoder Stage 2	0.91	0.86	0.79	0.114
Decoder Stage 3	0.94	0.90	0.84	0.111
Decoder Stage 4	0.95	0.92	0.87	0.109
Average	0.92	0.87	0.81	0.113

corresponding decoder update. We then measure how strongly the dominant feature subspace aligns with the dominant update directions. If low-rank feature structure indeed drives low-rank adaptation, layers with stronger concentration of feature energy in top principal components should also exhibit stronger concentration of update energy in top singular values.

As shown in Table 10, layers with stronger concentration of feature energy in the principal subspace also exhibit more strongly low-rank weight updates. This provides a more direct bridge between the PCA analysis of decoder features and the effectiveness of low-rank parameter updates such as LoRA.

H A Local Linearized Interpretation of Low-Rank Update Structure

In this section, we provide a simple mathematical interpretation linking low-dimensional decoder features to low-rank gradient and update structure. Our goal is not to claim a complete theory of the full nonlinear adaptation dynamics. Instead, we formalize what can be shown in an idealized linear regime, and then explain why the same intuition remains relevant as a local piecewise-linear interpretation for DPT-style decoders. This interpretation is consistent with our empirical findings that most adaptation benefit is preserved within a small principal decoder subspace, whereas orthogonal or random subspaces lead to substantially weaker adaptation, and that layers with stronger feature concentration also exhibit more strongly low-rank updates.

Linear layer. Consider a decoder layer with output

$$y = Wx, \quad W \in \mathbb{R}^{m \times d}, \quad x \in \mathbb{R}^d.$$

Let \mathcal{L} be a differentiable loss, and let

$$g := \frac{\partial \mathcal{L}}{\partial y} \in \mathbb{R}^m$$

denote the backpropagated error signal. By the chain rule, the gradient with respect to the layer weight is

$$\frac{\partial \mathcal{L}}{\partial W} = gx^\top.$$

Thus, the gradient is an outer product between the output-side error signal and the input feature.

Proposition 1 (Exact subspace-constrained gradient structure). *Assume that all input features x lie in an r -dimensional subspace $\mathcal{U} \subset \mathbb{R}^d$. Let $P \in \mathbb{R}^{d \times r}$ be a matrix whose columns form an orthonormal basis of \mathcal{U} . Then every feature can be written as*

$$x = Pz, \quad z \in \mathbb{R}^r.$$

Under this assumption, the gradient factorizes as

$$\frac{\partial \mathcal{L}}{\partial W} = gz^\top P^\top,$$

and therefore satisfies

$$\text{rank}\left(\frac{\partial \mathcal{L}}{\partial W}\right) \leq r.$$

Moreover, the row space of $\frac{\partial \mathcal{L}}{\partial W}$ is contained in \mathcal{U} .

Proof. Since $x = Pz$, substituting into

$$\frac{\partial \mathcal{L}}{\partial W} = gx^\top$$

gives

$$\frac{\partial \mathcal{L}}{\partial W} = g(Pz)^\top = gz^\top P^\top.$$

Because $gz^\top \in \mathbb{R}^{m \times r}$, we obtain

$$\text{rank}\left(\frac{\partial \mathcal{L}}{\partial W}\right) = \text{rank}(gz^\top P^\top) \leq r.$$

Also, right multiplication by P^\top implies that every row lies in $\text{span}(P) = \mathcal{U}$.

Proposition 2 (Approximate low-rank gradient structure). *Suppose each feature admits a decomposition*

$$x = Pz + \varepsilon,$$

where $P \in \mathbb{R}^{d \times r}$ has orthonormal columns and ε denotes the residual outside the principal subspace. Then the gradient decomposes as

$$\frac{\partial \mathcal{L}}{\partial W} = gz^\top P^\top + g\varepsilon^\top.$$

The first term has rank at most r , while the second term is a residual perturbation satisfying

$$\|g\varepsilon^\top\|_F = \|g\|_2 \|\varepsilon\|_2.$$

Hence, when the off-subspace residual is small, the gradient is well approximated by a rank- r matrix.

Proof. Substituting $x = Pz + \varepsilon$ into

$$\frac{\partial \mathcal{L}}{\partial W} = gx^\top$$

yields

$$\frac{\partial \mathcal{L}}{\partial W} = g(Pz + \varepsilon)^\top = gz^\top P^\top + g\varepsilon^\top.$$

The first term has rank at most r by the previous proposition. For the residual term,

$$\|g\varepsilon^\top\|_F^2 = \sum_{i,j} g_i^2 \varepsilon_j^2 = \|g\|_2^2 \|\varepsilon\|_2^2,$$

which implies

$$\|g\varepsilon^\top\|_F = \|g\|_2 \|\varepsilon\|_2.$$

Corollary 1 (Accumulated update structure). *Consider gradient-based updates over T steps:*

$$W_{t+1} = W_t - \eta_t G_t, \quad G_t = g_t x_t^\top.$$

If every feature satisfies $x_t \in \mathcal{U}$ for the same r -dimensional subspace \mathcal{U} , then the accumulated update

$$\Delta W_T := W_T - W_0 = - \sum_{t=0}^{T-1} \eta_t G_t$$

can be written as

$$\Delta W_T = A_T P^\top$$

for some matrix $A_T \in \mathbb{R}^{m \times r}$, and therefore

$$\text{rank}(\Delta W_T) \leq r.$$

In the approximate case $x_t = Pz_t + \varepsilon_t$, the accumulated update decomposes into a rank- r term plus a residual term controlled by

$$\sum_{t=0}^{T-1} \eta_t g_t \varepsilon_t^\top.$$

Proof. If $x_t = Pz_t$, then

$$G_t = g_t x_t^\top = g_t z_t^\top P^\top.$$

Therefore,

$$\Delta W_T = - \sum_{t=0}^{T-1} \eta_t g_t z_t^\top P^\top = A_T P^\top,$$

where

$$A_T := - \sum_{t=0}^{T-1} \eta_t g_t z_t^\top \in \mathbb{R}^{m \times r}.$$

Hence $\text{rank}(\Delta W_T) \leq r$. The approximate case follows by substituting $x_t = Pz_t + \varepsilon_t$ at each step.

Remark on nonlinear DPT decoders. The above statements are exact only for an idealized linear layer. Our actual decoder is nonlinear and includes operations such as multi-scale fusion, convolution, and ReLU activations. Therefore, we do not present the above propositions as an exact characterization of the full DPT decoder. However, ReLU networks are piecewise linear [31]: when the activation pattern is fixed, each local block behaves as an affine map. Under such a local view, the same subspace argument applies to the corresponding local Jacobian, implying that low-dimensional feature concentration biases the induced gradients and local update directions toward a low-rank structure, up to perturbations caused by activation-pattern changes and residual off-subspace energy.

Interpretation. Taken together, the above results do not constitute a complete theory of nonlinear test-time adaptation. Rather, they formalize a simple and conservative conclusion: if decoder features are concentrated in a low-dimensional principal subspace, then in a linearized or locally piecewise-linear regime, the corresponding gradients and accumulated updates are naturally biased toward low-rank structure. We view this as a local mechanistic interpretation that is consistent with our empirical findings, including the preservation of most adaptation gain within the top principal subspace and the observed alignment between feature covariance concentration and update low-rankness, rather than a global proof of the full nonlinear adaptation dynamics.

References

1. Bao, H., Dong, L., Piao, S., Wei, F.: Beit: Bert pre-training of image transformers. In: ICLR (2022)
2. Bartolomei, L., Poggi, M., Conti, A., Tosi, F., Mattoccia, S.: Revisiting depth completion from a stereo matching perspective for cross-domain generalization. In: 3DV. pp. 1360–1370. IEEE (2024)
3. Bhat, S.F., Alhashim, I., Wonka, P.: Adabins: Depth estimation using adaptive bins. In: CVPR. pp. 4009–4018 (2021)
4. Bhat, S.F., Alhashim, I., Wonka, P.: Localbins: Improving depth estimation by learning local distributions. In: ECCV. pp. 480–496. Springer (2022)
5. Birkl, R., Wofk, D., Müller, M.: Midas v3. 1—a model zoo for robust monocular relative depth estimation. arXiv preprint arXiv:2307.14460 (2023)
6. Bochkovskii, A., Delaunoy, A., Germain, H., Santos, M., Zhou, Y., Richter, S.R., Koltun, V.: Depth pro: Sharp monocular metric depth in less than a second. arXiv preprint arXiv:2410.02073 (2024)
7. Caron, M., Touvron, H., Misra, I., Jégou, H., Mairal, J., Bojanowski, P., Joulin, A.: Emerging properties in self-supervised vision transformers. In: ICCV. pp. 9650–9660 (2021)
8. Chen, X., Chen, X., Zha, Z.J.: Structure-aware residual pyramid network for monocular depth estimation. arXiv preprint arXiv:1907.06023 (2019)
9. Chodosh, N., Wang, C., Lucey, S.: Deep convolutional compressed sensing for lidar depth completion. In: ACCV. pp. 499–513. Springer (2018)
10. Conti, A., Poggi, M., Mattoccia, S.: Sparsity agnostic depth completion. In: WACV. pp. 5871–5880 (2023)

11. Eigen, D., Puhrsch, C., Fergus, R.: Depth map prediction from a single image using a multi-scale deep network. *NeurIPS* **27** (2014)
12. Fu, H., Gong, M., Wang, C., Batmanghelich, K., Tao, D.: Deep ordinal regression network for monocular depth estimation. In: *CVPR*. pp. 2002–2011 (2018)
13. Fu, X., Yin, W., Hu, M., Wang, K., Ma, Y., Tan, P., Shen, S., Lin, D., Long, X.: Geowizard: Unleashing the diffusion priors for 3d geometry estimation from a single image. In: *ECCV*. pp. 241–258. Springer (2024)
14. Geiger, A., Lenz, P., Stiller, C., Urtasun, R.: Vision meets robotics: The kitti dataset. *The international journal of robotics research* **32**(11), 1231–1237 (2013)
15. Guizilini, V., Ambrus, R., Pillai, S., Raventos, A., Gaidon, A.: 3d packing for self-supervised monocular depth estimation. In: *CVPR*. pp. 2485–2494 (2020)
16. Hao, Z., Li, Y., You, S., Lu, F.: Detail preserving depth estimation from a single image using attention guided networks. In: *3DV*. pp. 304–313. IEEE (2018)
17. He, K., Chen, X., Xie, S., Li, Y., Dollár, P., Girshick, R.: Masked autoencoders are scalable vision learners. In: *CVPR* (2022)
18. Hu, J., Ozay, M., Zhang, Y., Okatani, T.: Revisiting single image depth estimation: Toward higher resolution maps with accurate object boundaries. In: *WACV*. pp. 1043–1051. IEEE (2019)
19. Hyoseok, L., Kim, K.S., Byung-Ki, K., Oh, T.H.: Zero-shot depth completion via test-time alignment with affine-invariant depth prior. In: *AAAI* (2025)
20. Jeong, C., Bae, I., Park, J.H., Jeon, H.G.: Test-time prompt tuning for zero-shot depth completion. In: *ICCV*. pp. 9443–9454 (2025)
21. Jun, J., Lee, J.H., Lee, C., Kim, C.S.: Depth map decomposition for monocular depth estimation. In: *ECCV*. pp. 18–34. Springer (2022)
22. Ke, B., Obukhov, A., Huang, S., Metzger, N., Daudt, R.C., Schindler, K.: Repurposing diffusion-based image generators for monocular depth estimation. In: *CVPR*. pp. 9492–9502 (2024)
23. Koch, T., Liebel, L., Fraundorfer, F., Korner, M.: Evaluation of cnn-based single-image depth estimation methods. In: *Proceedings of the European Conference on Computer Vision Workshop (ECCVW)*. pp. 0–0 (2018)
24. Laina, I., Rupprecht, C., Belagiannis, V., Tombari, F., Navab, N.: Deeper depth prediction with fully convolutional residual networks. In: *3DV*. pp. 239–248. IEEE (2016)
25. Lee, J.H., Han, M.K., Ko, D.W., Suh, I.H.: From big to small: Multi-scale local planar guidance for monocular depth estimation. *arXiv preprint arXiv:1907.10326* (2019)
26. Leroy, V., Cabon, Y., Revaud, J.: Grounding image matching in 3d with mast3r. In: *ECCV*. pp. 71–91. Springer (2024)
27. Lin, H., Chen, S., Liew, J., Chen, D.Y., Li, Z., Shi, G., Feng, J., Kang, B.: Depth anything 3: Recovering the visual space from any views. *arXiv preprint arXiv:2511.10647* (2025)
28. Lin, H., Peng, S., Chen, J., Peng, S., Sun, J., Liu, M., Bao, H., Feng, J., Zhou, X., Kang, B.: Prompting depth anything for 4k resolution accurate metric depth estimation. In: *CVPR*. pp. 17070–17080 (2025)
29. Liu, Z., Cheng, K.L., Wang, Q., Wang, S., Ouyang, H., Tan, B., Zhu, K., Shen, Y., Chen, Q., Luo, P.: Depthlab: From partial to complete. *arXiv preprint arXiv:2412.18153* (2024)
30. Ma, F., Karaman, S.: Sparse-to-dense: Depth prediction from sparse depth samples and a single image. In: *ICRA*. pp. 4796–4803. IEEE (2018)

31. Montúfar, G., Pascanu, R., Cho, K., Bengio, Y.: On the number of linear regions of deep neural networks. *Advances in neural information processing systems* **27** (2014)
32. Niu, S., Wu, J., Zhang, Y., Wen, Z., Chen, Y., Zhao, P., Tan, M.: Towards stable test-time adaptation in dynamic wild world. *arXiv preprint arXiv:2302.12400* (2023)
33. Oquab, M., Darcet, T., Moutakanni, T., Vo, H.V., Szafraniec, M., Khalidov, V., Fernandez, P., HAZIZA, D., Massa, F., El-Nouby, A., Assran, M., Ballas, N., Galuba, W., Howes, R., Huang, P.Y., Li, S.W., Misra, I., Rabbat, M., Sharma, V., Synnaeve, G., Xu, H., Jegou, H., Mairal, J., Labatut, P., Joulin, A., Bojanowski, P.: DINOv2: Learning robust visual features without supervision. *TMLR* (2024)
34. Park, J., Joo, K., Hu, Z., Liu, C.K., So Kweon, I.: Non-local spatial propagation network for depth completion. In: *ECCV*. pp. 120–136. Springer (2020)
35. Piccinelli, L., Sakaridis, C., Yang, Y.H., Segu, M., Li, S., Abbeloos, W., Van Gool, L.: Unidepth2: Universal monocular metric depth estimation made simpler. *arXiv preprint arXiv:2502.20110* (2025)
36. Piccinelli, L., Yang, Y.H., Sakaridis, C., Segu, M., Li, S., Van Gool, L., Yu, F.: Unidepth: Universal monocular metric depth estimation. In: *CVPR*. pp. 10106–10116 (2024)
37. Ren, Z., Zhang, Z., Li, W., Liu, Q., Tang, H.: Anydepth: Depth estimation made easy. *arXiv preprint arXiv:2601.02760* (2026)
38. Seo, M., Hamilton, M., Kim, C.: Upsample anything: A simple and hard to beat baseline for feature upsampling. *arXiv preprint arXiv:2511.16301* (2025)
39. Silberman, N., Hoiem, D., Kohli, P., Fergus, R.: Indoor segmentation and support inference from rgb-d images. In: *ECCV*. pp. 746–760. Springer (2012)
40. Siméoni, O., Vo, H.V., Seitzer, M., Baldassarre, F., Oquab, M., Jose, C., Khalidov, V., Szafraniec, M., Yi, S., Ramamonjisoa, M., et al.: Dinov3. *arXiv preprint arXiv:2508.10104* (2025)
41. Tang, J., Tian, F.P., An, B., Li, J., Tan, P.: Bilateral propagation network for depth completion. In: *CVPR*. pp. 9763–9772 (2024)
42. Uhrig, J., Schneider, N., Schneider, L., Franke, U., Brox, T., Geiger, A.: Sparsity invariant cnns. In: *3DV*. pp. 11–20. IEEE (2017)
43. Viola, M., Qu, K., Metzger, N., Ke, B., Becker, A., Schindler, K., Obukhov, A.: Marigold-dc: Zero-shot monocular depth completion with guided diffusion. In: *ICCV*. pp. 5359–5370 (2025)
44. Wang, J., Chen, M., Karaev, N., Vedaldi, A., Rupprecht, C., Novotny, D.: Vggg: Visual geometry grounded transformer. In: *CVPR*. pp. 5294–5306 (2025)
45. Wong, A., Fei, X., Tsuei, S., Soatto, S.: Unsupervised depth completion from visual inertial odometry. *IEEE Robotics and Automation Letters (RA-L)* **5**(2), 1899–1906 (2020)
46. Yang, L., Kang, B., Huang, Z., Xu, X., Feng, J., Zhao, H.: Depth anything: Unleashing the power of large-scale unlabeled data. In: *CVPR*. pp. 10371–10381 (2024)
47. Yang, L., Kang, B., Huang, Z., Zhao, Z., Xu, X., Feng, J., Zhao, H.: Depth anything v2. *NeurIPS* **37**, 21875–21911 (2024)
48. Yin, W., Liu, Y., Shen, C., Yan, Y.: Enforcing geometric constraints of virtual normal for depth prediction. In: *ICCV*. pp. 5684–5693 (2019)
49. Yin, W., Zhang, C., Chen, H., Cai, Z., Yu, G., Wang, K., Chen, X., Shen, C.: Metric3d: Towards zero-shot metric 3d prediction from a single image. In: *ICCV*. pp. 9043–9053 (2023)

50. Yuan, W., Gu, X., Dai, Z., Zhu, S., Tan, P.: New crfs: Neural window fully-connected crfs for monocular depth estimation. arXiv preprint arXiv:2203.01502 (2022)
51. Zhang, Y., Guo, X., Poggi, M., Zhu, Z., Huang, G., Mattoccia, S.: Completion-former: Depth completion with convolutions and vision transformers. In: CVPR. pp. 18527–18536 (2023)
52. Zhou, J., Wei, C., Wang, H., Shen, W., Xie, C., Yuille, A., Kong, T.: ibot: Image bert pre-training with online tokenizer. In: ICLR (2022)
53. Zuo, Y., Deng, J.: Ogni-dc: Robust depth completion with optimization-guided neural iterations. In: ECCV. pp. 78–95. Springer (2024)